Yu Zhuang · Qiang Xu · Aiguo Xing · Muhammad Bilal · Kaushal Raj Gnyawali

Catastrophic air blasts triggered by large ice/rock avalanches

Abstract Large ice/rock avalanches have been known to generate extremely powerful air blasts capable of causing fatalities and destruction far beyond the runout of the movement mass. Thus, an appraisal of their possible destructive air blast should be considered during the risk assessments. However, much less is known about how avalanche-induced air blasts occur and how destructive they are. Here an existing DEM-CFD coupled method was innovatively employed to quantitatively analyze the initiation and propagation mechanism of the air blast caused by the largest ice-rock avalanche during Nepal's 2015 Gorkha earthquake, and compared the results with some recorded events. Our results highlighted the contribution of valley morphology to air blast generation. Large high-velocity ice/rock avalanches that have an airborne trajectory or a travel path with turning points can suddenly release tremendous energy and more probably cause destructive air blasts. Additionally, the Langtang air blast presented a propagation of 1 km from the avalanche impact point and equivalent destruction to an EF2–EF5 tornado, causing mass casualties. The large impact region and destructive force of avalanche-induced air blasts suggests their disastrous consequences that should provoke assessment of such type of cascading effect during the landslide risk assessment, especially for the long-term sustainability of planned infrastructure in high-altitude regions.

Keywords Ice/rock avalanche · Air blast · DEM-CFD coupled modeling · Disaster-causing mechanism

Introduction

Large ice/rock avalanches (hereinafter named avalanche) involve a massive amount of energy and can be extremely hazardous owing to their long-runout distance, high mobility, and possible chain disaster (Mulligan et al. 2020; Shugar et al. 2021; Zhang et al. 2022). A moving avalanche with a large volume and high velocity can suddenly release tremendous energy into the surrounding air, and generate a powerful air blast that is capable of flattening buildings, uprooting trees, and lifting vehicles and people into the air (Adams 1881; Zimmer et al. 2012). In recent decades, destructive avalanche-induced air blasts have frequently occurred in high-altitude regions and caused mass casualties and economic loss (Fig. 1). Unfortunately, to date, no ice/rock avalanche hazard and risk assessment have accounted for the potential air blast (Penna et al. 2021). Preventing and mitigating disasters caused by such type of cascading events is now a novel but urgent problem.

Much effort has been made to research the dynamic characteristics of snow avalanche-induced air blasts (e.g., Dreier et al. 2016; Bartelt et al. 2018; Caviezel et al. 2021). However, little attention has been paid to the risk associated with the air blast results

from the ice/rock avalanche. Most research just describes the air blast phenomenon (Wang et al. 2009; Yin and Xing 2012; Lacroix 2016) or estimates the air blast velocity based on the Beaufort and TORRO Tornado Intensity Scale (Wieczorek et al. 2000; Kargel et al. 2016). These efforts are valuable in providing us with a preliminary understanding of the power of the avalanche-induced air blast, while further in-depth research needs to be conducted on its initiation mechanism and propagation process. Nevertheless, the avalanche impact properties and near-field air blast characteristics in high-altitude regions are hardly observable (He et al. 2018), and the monitoring equipment can also get damaged because of the far-field destruction of the generated air blast. Therefore, investigations of avalanche-induced air blast dynamics in a real event need to be based on numerical modeling with a complex three-dimensional tomography, which will aid in the landslide risk assessment and the proposition of appropriate measures. To our knowledge, although great efforts have been made to model the snow avalanche-induced air blasts (e.g., Christen et al. 2010; Buser and Bartelt 2015; Bartelt et al. 2016), very few studies have provided a three-dimensional numerical analysis of recorded ice/rock avalanche-induced air blasts to date (Zhuang et al. 2019). Notably, the above snow avalanche-induced air blast models are mostly established based on the two-layer theory. The dense avalanche core consisting of snow particles with low density and small grain size (Skiles and Painter 2017) is regarded as fluid, while the air blast is generated by air expelled from the core. Such models have the advantage of low time-costing and show good performance in simulating the air blast near the core, but the results are comparatively weak for deflection and far-field propagation in a 3-D air blast model. As for the ice/rock avalanches, the movement process of ice/rock mass with large particle size involves complicated solid–solid and solid-air interactions. Developing an applicable numerical method is therefore essential for air blast modeling and investigating the criteria that must be met for a destructive ice/rock avalanche-induced air blast.

This study innovatively used a discrete element method-computational fluid dynamics (DEM-CFD) coupled method to quantitatively analyze the destructive air blast triggered by the largest ice-rock avalanche (Langtang avalanche) during Nepal's 2015 Gorkha earthquake, and compared it with recorded events from around the world. The Langtang event is a rare case as over 350 deaths were primarily caused by the generated air blast. We further synthesized the generation modes and key control factors of destructive avalanche-induced air blasts. The new insights into the initiation and propagation mechanism of avalanche-induced air blasts open new perspectives for the landslide risk assessment in high-altitude regions, especially for regions with a similar

Fig. 1 Post-disaster view of recent destructive avalanche-induced air blasts. **a** Trees with a diameter over 1 m snapped by the Yigong avalanche-induced air blast in 2000 (Yin and Xing 2012). **b** Trees damaged by the Wenjia valley avalanche–induced air blast in 2008 (Zhuang et al. 2019). **c** Buildings flattened by the disastrous West Town avalanche-induced air blast in 2008 (Yin 2014). **d** Forest of small trees flattened by the Yumthang avalanche-induced air blast in 2015 (Penna et al. 2021)

condition to the Qinghai Tibet Plateau in China, where a large number of infrastructures including high-speed railways, roads, bridges, and hydropower stations will be built in disaster-prone regions with high altitudes (Ni et al. 2021).
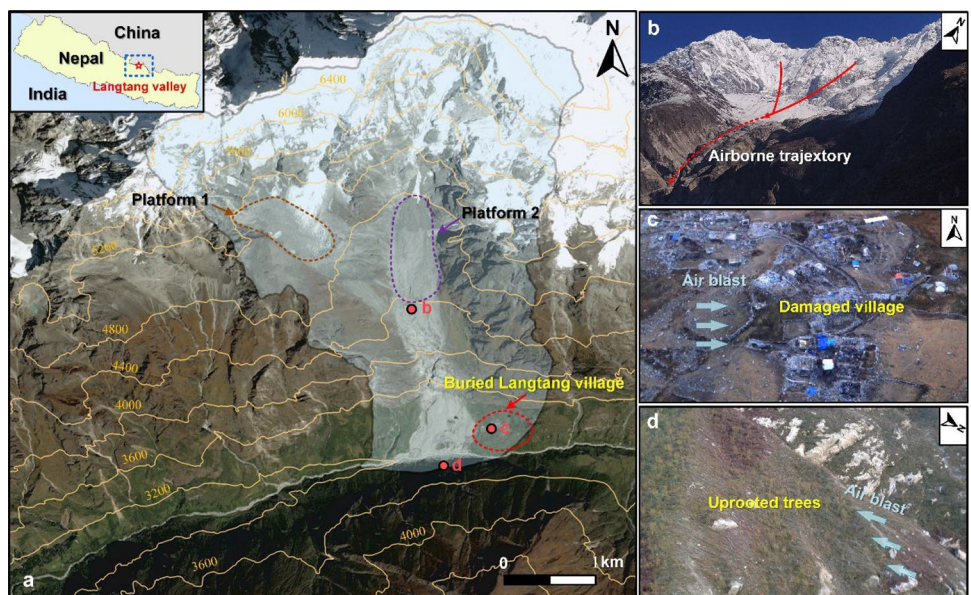
Langtang debris avalanche

Among the numerous landslides triggered by the Gorkha earthquake in central Nepal, the mixed ice-rock debris avalanche that occurred in the Langtang valley is the largest and most catastrophic event (28°12′55.43″N, 85°30′8.95″E) (Fig. 2a). The Langtang valley is a famous trekking course for tourists in the Himalayas with a

tectonically active mountain belt, approximately 60 km north of Kathmandu. Nevertheless, the destructive air blast triggered by the debris avalanche buried the well-known touristic village of Langtang and destroyed a large part of this valley. At least 350 people were killed or left missing in this destructive disaster (Kargel et al. 2016).

The Langtang debris avalanche involves an area of approximately 15 km², a total estimated volume of 14.38×10^6 m³, and a runout distance of over 5 km, whose source materials detached from the top region of the mountain at the highest altitude of ~7000 m a.s.l. and deposited in the Langtang River at an altitude

Fig. 2 a Overview of the Langtang avalanche. The blue shaded region indicates the impact area of the Langtang avalanche. Red dots show the locations of panels **b**–**d**. **b** Edge of the platform where the avalanche became airborne. **c** Buildings damaged by the Langtang avalanche-induced air blast. **d** Trees uprooting observed on the opposite slope

of 3200 a.s.l. The debris avalanche is composed mainly of ice, and the rock mass volume was estimated to be 1.84×10^6 m³ (Gnyawali et al. 2020). An evident snowline was observed at 5000 m a.s.l. according to the satellite images captured covered the landslide period (through April to May 2015), and the rock mass below the snowline are various types of gneisses and granitic migmatites. Notably, two low-gradient platforms (platforms 1 and 2 marked in Fig. 2a) exist at the intersection of the snow-ice fallout zone and rock debris talus zone.

The interpretation results of the satellite image reveal that the primary event of the Langtang debris avalanche was a series of ice-snow debris detaching from multiple source areas near 7000 m a.s.l. under moderate ground shaking of 0.26 g. Afterwards, the ice-snow debris descended downhill, entrained the rock mass along the travel path, and generated the ice-snow-rock mixed debris avalanche. The avalanche mass then became partially airborne for ~ 500 m as it fell off the platform at an altitude of 4500 m (Fig. 2b), and many villagers witnessed the "black avalanche" (Fujita et al. 2017). After the debris avalanche fell below the Langtang village at 4000 m and the riverbed at 3200 m, it climbed up the opposite mountain ~ 200 m. The subsequent air blast (generated at the impact point) further propagated 400 m up the mountain and 1 km up and down the valley from the impact point on the valley floor (Kargel et al. 2016). As per observers, the air blast was so powerful that it destroyed houses constructed of stone slabs and even flattened a small forest (Fig. 2c and d). The Langtang event is a rare case in which the casualties and building damages primarily resulted from the air blast, not from the avalanche.

Data and methods

DSM generation

Two tri-stereo SPOT6/7 images covering the Gorkha earthquake period were acquired in the Langtang valley over 100 km². We summarized here the main method for DSM generation (Lacroix 2016). The images have a very high resolution (1.5 m) and are suitable for hazard studies over a large region or with a small size, typically for Langtang debris avalanche with multiple source materials at different locations. Based on the tri-stereo images, two digital surface models (DSM) were reconstructed in April 2014 and in May 2015 (15 days after the Langtang debris avalanche), respectively. The DSMs were obtained using the NASA open-source software Ames Stereo Pipeline. Images were first map-projected using the low-resolution SRTM DSM, and boudle-adjusted through automatically extracted tie points. Afterwards, the triangulation step was realized jointly with all the images. A point cloud of the surface topography was then generated and transformed as a grid with a regular spacing of 4 m, approximately 3 times the initial satellite resolution.

DEM-CFD coupling method

A 3D DEM-CFD (EDEM-Fluent) coupling simulation was performed to analyze the runout behavior of the debris avalanche and the propagation process of the associated air blast. EDEM (DEM Solutions Ltd 2019) and Fluent (ANSYS Inc 2018) calculated the dynamic characteristics of the debris avalanche and generated air blast, respectively, while an application programming interface (API) played a role in converting momentum and energy between these two phases.

DEM can be implemented to numerically quantify contact forces, velocities, and displacements of an assembly of particles based on the specific contact model and Newton's second law. The particle-to-particle contact leads to calculating the normal and tangential forces between particles, while the interaction between particles and geometry helps distinguish the impact of real geometry on particle motion. Here, the Hertz-Mindlin contact model (Hertz 1882; Mindlin 1949) was selected in the EDEM to obtain the intact force between particles because of its accuracy and efficiency in representing the granular flow (debris avalanche). Furthermore, the air blast propagation simulation was performed using a CFD code Fluent by employing the Navier–Stokes equation. In this study, we used the RNG k-ɛ Model (Yakhot and Orszag 1986) to solve the equations and the Eulerian multiphase fluid model to calculate the interactions between multiple phases (the sliding mass was modeled as a fluid in Fluent), so that the dynamic characteristics of the air blast can be determined. Importantly, the coupling interface (API) enables the synchronous work of two separate programs by making the transmitted data act as the drag force (Eq. 1).

$$F_g = \pi d_p^2 C_d \left(v_g - v_p \right) \left| v_g - v_p \right| / 8 \qquad (1)$$

where d_p is the particle diameter, C_d presents the drag coefficient, and v_g and v_p is the velocities for the fluid and particles, respectively.

When the coupled simulation initiates, the Ansys Fluent code simulates first and transfers all related data to EDEM through the API at each time step. Subsequently, the liquid drag forces and corresponding torques are incorporated into particle simulations in the EDEM in addition to the gravitational force and collision impact on the particles. The calculated particle data then transmits to the Fluent again through the API, updates the status of the fluid, and completes one coupling calculation. The coupled simulation processes through transforming data between Fluent and EDEM at each specific time step and eventually calculating the dynamic characteristics of debris avalanche and associated air blast.

Numerical modeling of avalanche-induced air blast dynamics is a major challenge, as complicated solid–solid and solid–fluid interactions would be involved. The DEM-CFD coupling method can greatly represent the interactions between ice/rock mass and the surrounding air and account for the outrush of air through the avalanche. We chose the EDEM-Fluent coupling method in this study because it is complex enough to represent the essential process of avalanche movement and air blast propagation, and mature that has been validated in the field of avalanche-associated chain disasters (Bilal et al. 2021).

Numerical model and parameters

In our numerical analysis, we first used ArcGIS (ESRI Inc 2019) to establish a digital elevation model (DEM) of the real 3D tomography with a size of 7 km × 7 km, which is applicable for the EDEM-Fluent simulation. The ICEM (ANSYS Inc 2018) was then employed to generate the geometry mesh of the landslide region. The computational domain was discretized using the unstructured tetrahedral mesh and comprised more than 500 million elements with a

nominal size of 15 m. Subsequently, EDEM generated particles in the predetermined source areas, which are the same as the real condition, and started the simulation. The generated particles accelerated along the travel path and transferred the energy to the surrounding air (transfer EDEM data into Fluent by the coupling interface). Input parameters for the numerical models are based on in situ measurements made at the field site and values obtained from the published literature, as presented in detail in Table 1. Gnyawali et al. (2020) measured the rock particle size to be 0.6–5.0 m. However, modeling real landslide cases with actual particle numbers and sizes is hardly feasible because of the large number of particles and enormous computational power. Balancing the solution accuracy of the numerical model and computational time costs, particle sizes of 2.0 m for ice and 2.0–5.0 m for the rock mass are selected for the numerical work. The density of ice and rock mass is determined based on the work conducted by Fujita et al. (2017) and Gnyawali et al. (2020), air-related parameters (density ρ_a and viscosity μ_a) are determined according to Gao and Zhang (2021), and the remaining parameters listed in Table 1 are obtained by conducting a back analysis. Furthermore, the locations and volumes of source areas are obtained based on the interpolation of pre- and post-DEMs. Thus, we believe that the model presented in this study could represent

the essential processes of the Langtang avalanche. Notably, our work primarily focused on the runout behavior of the avalanche and the dynamic characteristics of the generated air blast. Thus, the failure mechanism analysis was not involved in the numerical work.

Results

The coupled CFD-DEM simulation results of the Langtang avalanche-induced air blast are presented in Figs. 3, 4, 5, 6, 7, and 8. The avalanche has a duration of approximately 144 s and moved with an average velocity of 37 m/s. The maximum velocity of over 100 m/s was calculated at the toe of the mountain (where an airborne trajectory was identified). Furthermore, the significant air blast was generated at the impact point on the valley floor with an initial velocity of over 80 m/s, and then propagated 1 km up and downstream the valley within 50 s. The detailed simulation results are as follows.
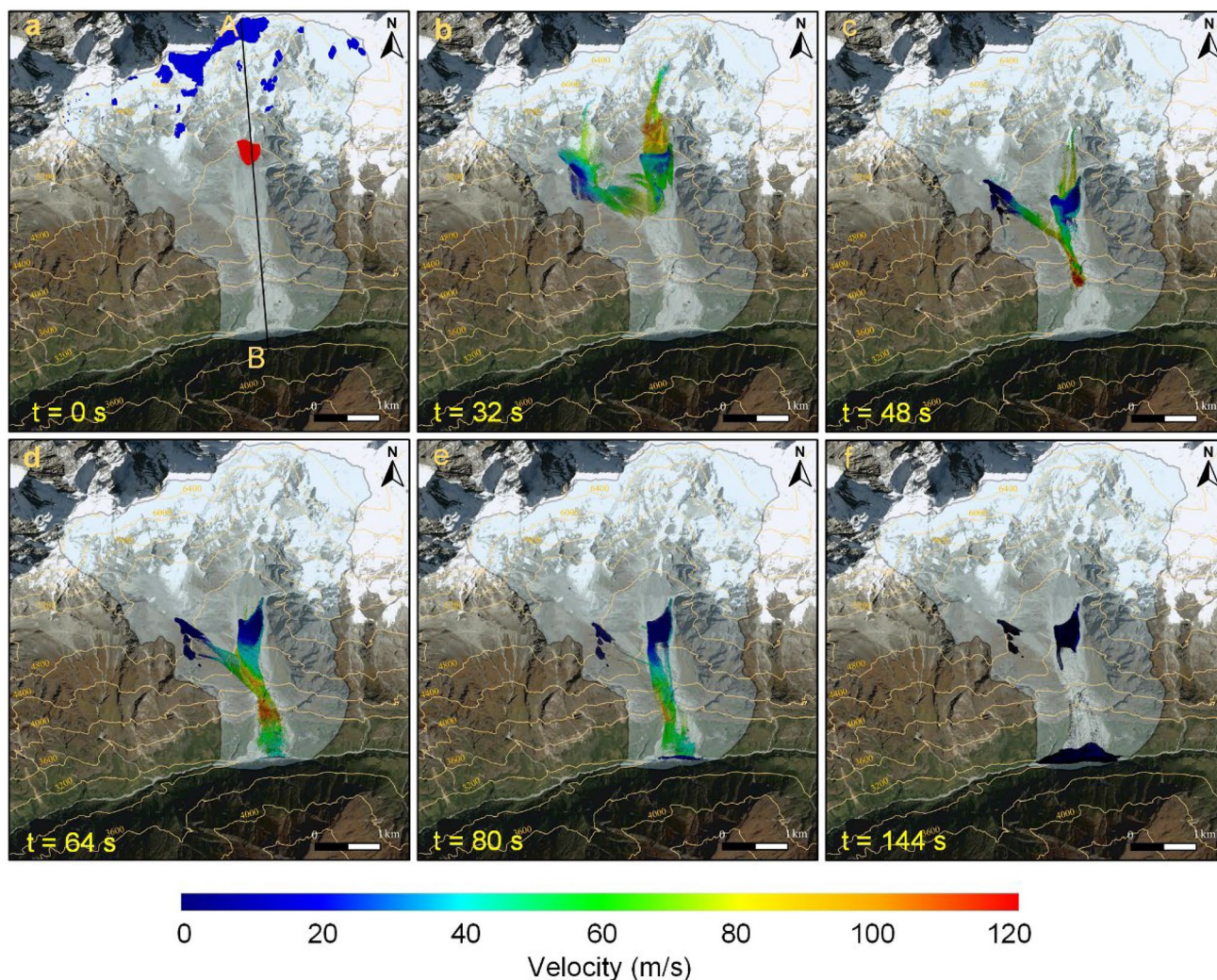
Stages of the debris avalanche

Figure 3 shows the runout behaviors of the sliding mass during the overall runout of the Langtang avalanche. In the initiation of the event, the ice-snow materials from multiple source areas were destabilized by the earthquake, moving downward independently, and gradually forming two branches of the avalanche. The main part of right branch (upper left part in Fig. 3b) deflected the moving path at platform 1, while the left branch (upper right part in Fig. 3b) of the ice-snow mixture started to entrain the rock materials at platform 2. Subsequently, two branches of avalanches began to converge and continuously entrained the rock materials below 5000 m a.s.l., eventually forming the ice-snow-rock mixed debris avalanche. The mixed avalanche then became airborne as it fell off a cliff below 4500 m. The steep topography and airborne trajectory caused the high velocity of the avalanche in the region, and a maximum velocity of 109 m/s was recorded at the impact point (Fig. 3c). After falling into the Langtang valley, the mixed avalanche propagated through the valley to the opposite slope (Fig. 3d) and blocked the Langtang river (Fig. 3e). A maximum velocity of approximately 60 m/s was identified at the front margin when the avalanche reached the opposite slope, and then, the run-up and splashing occurred. The velocity value at this specific point matches Kargel's estimation well (63 m/s). Eventually, the avalanche was deposited in the Langtang valley with parts remaining on both platforms (Fig. 3f), showing high agreement with the deposit feature described by Nagai et al. (2017) and Fujita et al. (2017).

Stages of the air blast

Figures 4 (air blast velocity) and 5 (air blast pressure) present the initiation and propagation process of the Langtang avalanche-induced air blast along the section line A-B. Air blast is identified during the whole avalanche moving process, and the most significant phenomenon is recorded at the end of the airborne trajectory. The generated air blast shows an increasing velocity between 48 and 64 s near the impact point (generation stage) with a maximum velocity of over 80 m/s, corresponding to the time step when the main part of the avalanche fell to the valley floor. The maximum relative pressure reaches over 9 kPa near the impact point at the

Table 1 Input parameters for the Langtang avalanche and induced air blast

|	Symbol	Value	Description
DEM	D_s	2–5 m	Rock particle diameter
	Di	2 m	Ice particle diameter
	ρ_s	2600 kg/m³	Rock mass density
	ρi	850 kg/m³	Ice mass density
	e_r	0.45	Co-efficient of restitution (rock)
	R_{rs}	0.35	Co-efficient of rolling resistance (rock)
	R_{rr}	0.25	Co-efficient of static resistance (rock)
	e_i	0.35	Co-efficient of restitution (ice)
	R_{is}	0.25	Co-efficient of rolling resistance (ice)
	R_{ir}	0.2	Co-efficient of static resistance (ice)
	g	9.81 m/s²	Gravitational acceleration
	Δt	1×10⁻⁴ s	DEM time step
CFD	Δt	1×10⁻² s	CFD time step
	ρ_a	1.225 kg/m³	Air density
	μ_a	17.9×10⁻⁶ Pa s	Air viscosity
	C_{1e}	1.42	RNG k-ε model constant
	C_{2e}	1.68	RNG k-ε model constant
	C_μ	0.0845	RNG k-ε model constant

Fig. 3 Displacement and velocity evolution of the Langtang debris avalanche. **a–f** show the avalanche velocity at 0 s, 32 s, 48 s, 64 s, 80 s, and 144 s, respectively. The ice-snow mass is presented in blue colour, while the rock material below 5000 a.s.l. is presented in red colour on platform 2, as shown in a. Line A-B indicates the main runout direction of the Langtang event

stage. The air blast then rapidly propagated through the valley and reached the riverbed with a front velocity of over 45 m/s. In the following 64 s (64–128 s, propagation stage), the high-velocity air blast ran up against the opposite slope with strong destructive power. The wind velocity and pressure are quite high in the stage and a maximum value of over 60 m/s and 6.0 kPa, respectively, are identified at 128 s, flatting the forests within the damage region. Afterwards (128–144 s, dissipation stage), the air blast concentration on the opposite slope started to dissipate as it travelled further away from the birthplace, and the main part of the avalanche stopped moving (no more energy was transferred to the air). The maximum run-up of the air blast reached up to 650 m.

We further analyzed the air blast propagation along the Langtang valley, as presented in Fig. 6 (3D representation of the air blast maximum velocity in the horizontal section at 50 m height above the valley floor). The air blast was concentrated near the impact point with a maximum velocity of over 80 m/s, then travelling toward the opposite slope (Fig. 6a and b). When its front margin reached the opposite slope, the violent impact resulted in the lateral spreading effect, forcing the air blast to propagate in both directions of the Langtang valley. Subsequently, the deflected air blast rapidly moved upstream and downstream along the opposite slope with a front velocity of approximately 40 m/s in both directions (Fig. 6c–e). Interestingly, we did not observe a significant decrease of wind velocity in this stage, even the induced air blast has travelled hundreds of meters away from the impact point. This phenomenon confirms the significant impact of avalanche impact duration, as the sustained energy was transferred for the further propagation of the air blast. Eventually, the air blast began to dissipate as the main part of debris avalanche has deposited in the valley (Fig. 6f). The simulated air blast presented a damage region of approximately 1 km up and down the valley and shows similar results to prior helicopter investigations employed by Collins & Jibson (2015) and Kargel et al. (2016) (1 km up and down the valley and run-up of 600 m up the opposite mountain). Moreover, we further verified the air blast results by estimating the wind velocity according to the post-disaster scene. Air blasts leveled the houses that were not buried by the avalanche and flattened a small forest
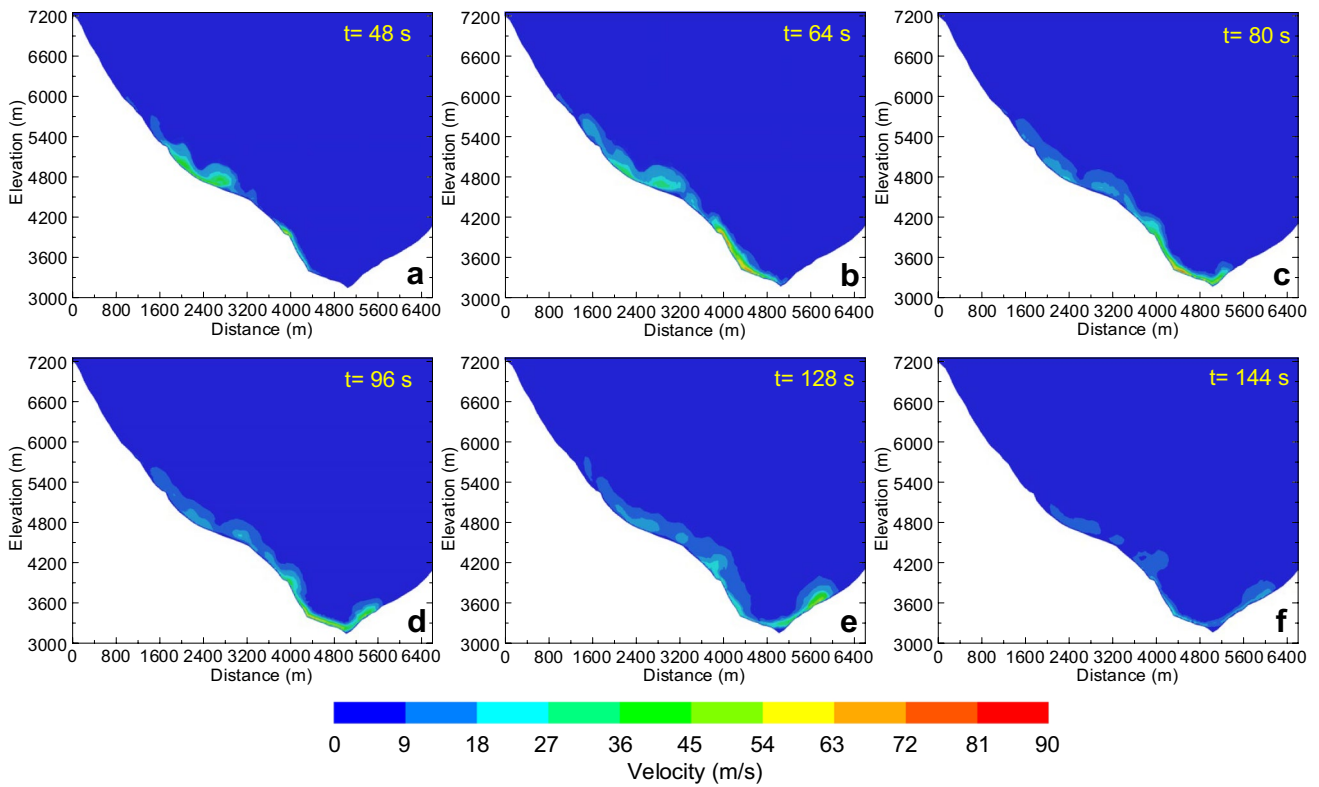
Fig. 4 Evolution of the Langtang avalanche-induced air blast velocity along section A-B
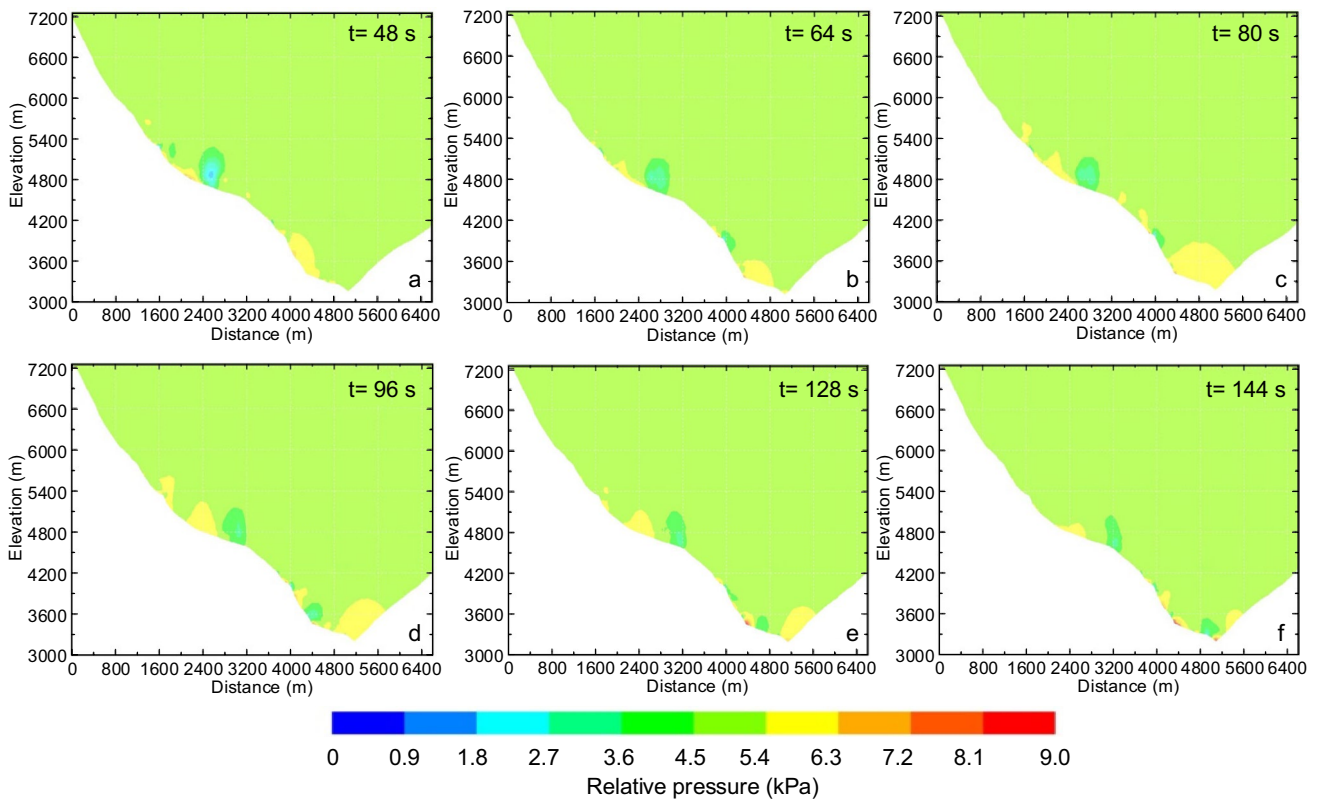
Fig. 5 Evolution of the Langtang avalanche-induced air blast pressure along section A-B
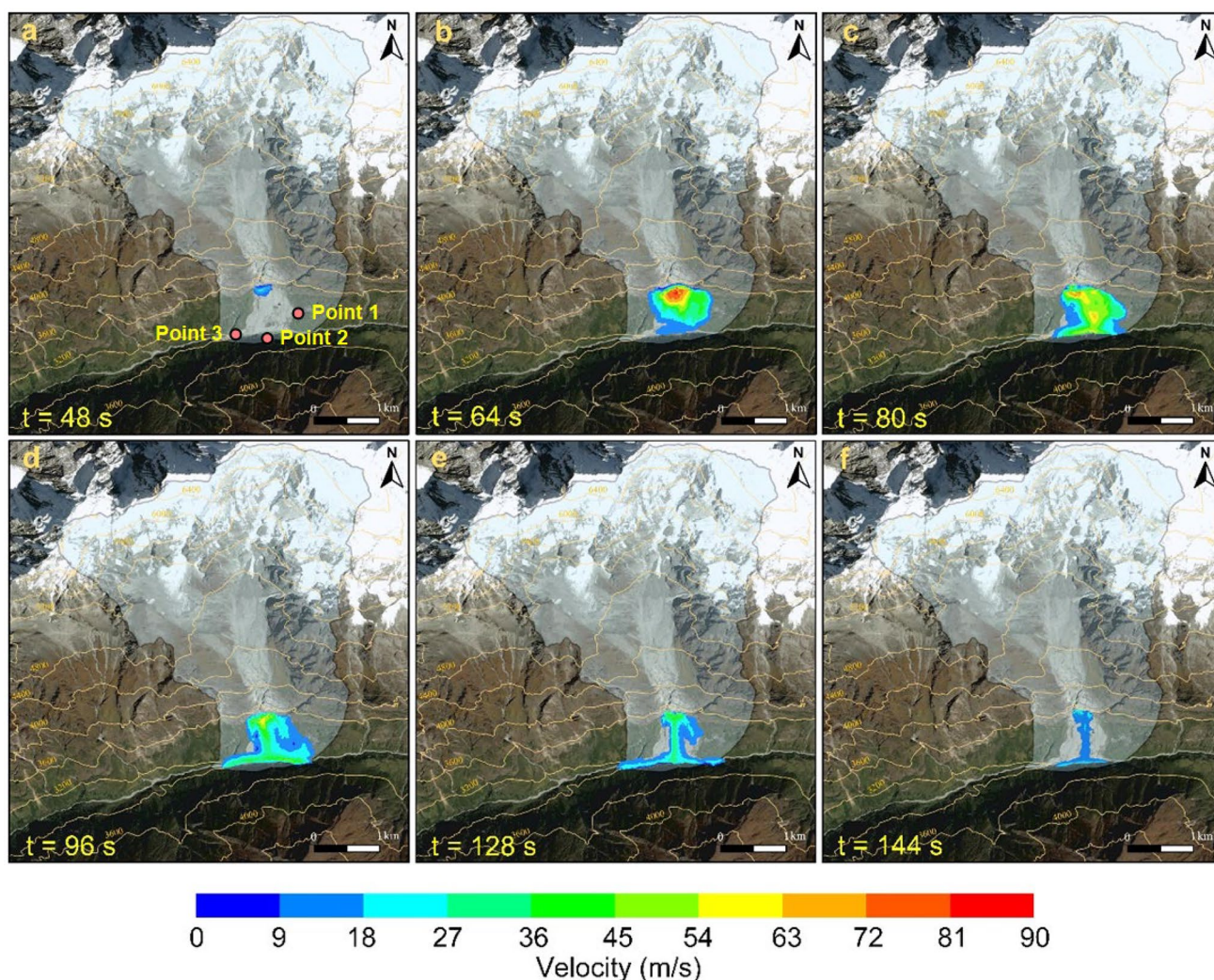
Fig. 6 Evolution of the Langtang avalanche-induced air blast along the valley (the horizontal section at 50 m elevation above the valley floor). **a–f** show the air blast velocity at 48 s, 64 s, 80 s, 96 s, 128 s, and 144 s, respectively. Points 1, 2, 3 indicate the monitoring points at the Langtang village, the opposite mountain, and the downstream of valley, respectively

on the opposite slope, suggesting wind speeds comparable with an ER5 tornado (> 89 m/s wind speed) in the Langtang village and ER2 tornado (49–60 m/s wind speed) on the opposite slope (Kargel et al. 2016). Both values highly agree with our numerical results (i.e., over 80 m/s in the Langtang village and 45–60 m/s on the opposite slope).

Three monitoring points were set up in the Langtang village (point 1), the opposite slope (point 2, 400 m height above the valley floor) and the Langtang valley (point 3), respectively, to quantitatively analyze the pressure variation and power of the air blast (Fig. 7). The monitoring results presented a maximum air pressure of over 7.5 kPa near the Langtang village, 6.1 kPa on the opposite slope, and 5.0 kPa in the Langtang valley. The modeled air pressure is also in good agreement with eyewitness observations of the infrastructure damage in the Langtang village and forest damage in the valley. Notably, the positive air pressure at the Langtang village existed for approximately 90 s as the impact between the avalanche and the slope lasted about 90 s. According to the simulated air blast velocity (v), the equation of Bernoulli stagnation pressure

can further be used to simply estimate the air blast pressure (p) (Houghton and Carpenter 2003):

$$p = k \cdot 0.5 \cdot \rho \cdot v^2 \qquad (2)$$

where k is the dimensionless stagnation pressure coefficient and ρ is the density of air. Numerical results indicated that the maximum velocities at points 1–3 are 71 m/s, 62 m/s, and 55 m/s, respectively. Compared with the simulated air blast pressure shown in Fig. 7, a k value of 2.5 illustrates a good estimated result here (7.7 kPa, 5.9 kPa, and 4.6 k Pa, respectively, for points 1–3).

The model-simulated maximum velocity at different heights indicates the vertical impact region of the air blast (Fig. 8). The Langtang avalanche-induced air blast is powerful within 150 m above the valley floor (Fig. 8a and b), while velocity attenuation is easily observed with height increase. Nevertheless, a maximum velocity of over 50 m/s still remained at the impact point and the opposite slope even at the height of 500 m above the valley floor (Fig. 8c), which corresponds to the destruction of the ER2 tornado, showing the large vertical damage region of the generated air blast.
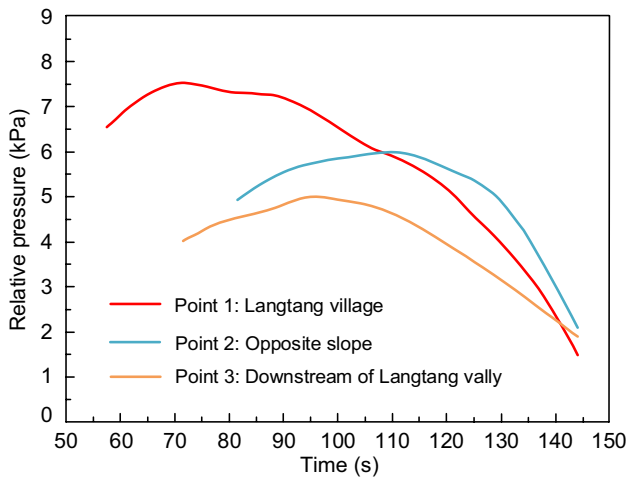
Fig. 7 Variation of air blast pressure at monitoring points. Locations of the monitoring points are presented in Fig. 6a. Points 1–3 are located in the Langtang village, the opposite slope (400 m above the valley floor) and downstream of Langtang valley, respectively
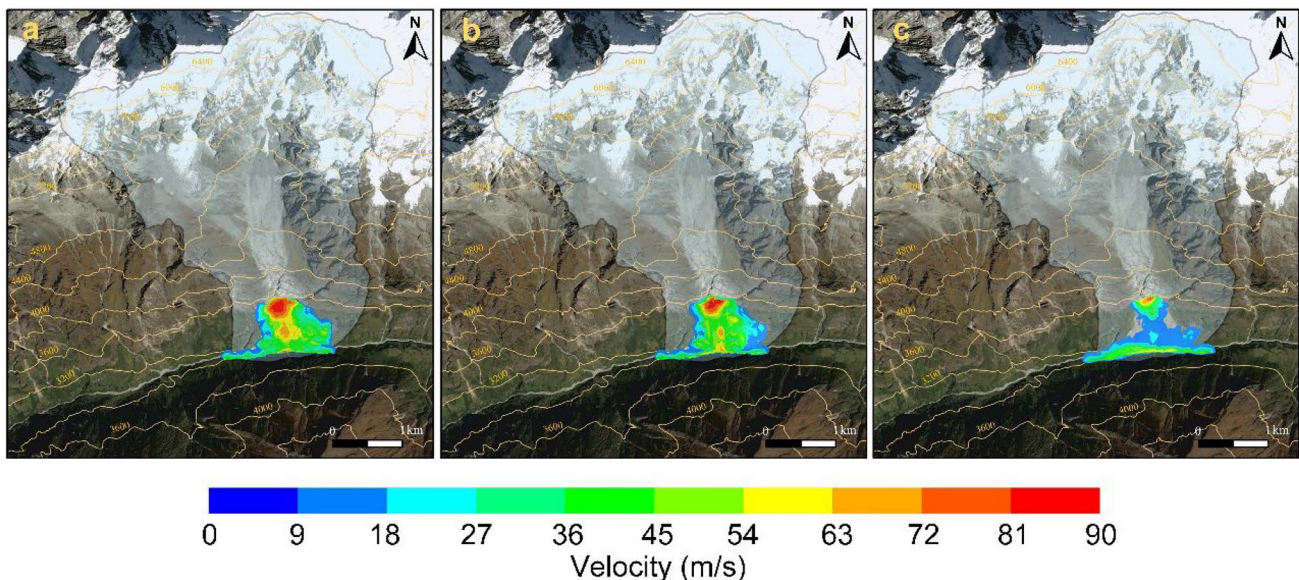
Additionally, the maximum velocity contour along with both directions of the valley further confirmed the contribution of the avalanche impact duration, as the air blast has a uniform maximum velocity along the propagation path (in the valley) and dissipates in a short time.

Discussion

Initiation mechanism

De Blasio et al. (2018) pointed out that for extremely energetic rockfalls (a large fall height of over 300 m; a large volume of over 10,000 m³, and a sudden release of energy), the impact after a free fall causes immediate release of energy much like an explosion, and numerous energy goes into prompt fragmentation and blast. The generated air blast could snap trees hundreds of meters ahead of the fall area. Nevertheless, how could ice/rock avalanches generate destructive air blasts is questionable because of the long-duration interaction with the ground without a sudden release of energy. Many long-runout avalanches in the high-altitude region involve a large volume and move downward with a large elevation difference. Yet they mostly move forward along moderate to gentle slopes, dissipating energy along the travel path without a violent impact and could not induce a powerful air blast. Therefore, the air blast phenomenon is commonly identified in many avalanches, but they always cause only minor destruction in comparison to the avalanche. For instance, our investigation result of the Shuicheng long runout rock avalanche that occurred in Guizhou China shows a slight air blast. The rock avalanche involved a volume of 2 Mm³ and caused 52 casualties, while the generated air blast just blew down a few corn plants at the front of the deposit area (Zhuang et al. 2021). This probably explains why little attention has been paid to air blasts during the landslide risk assessment. However, our work on the Langtang debris avalanche shows different results. The Langtang debris avalanche became airborne for at least 500 m from a cliff below 4500 m (downstream of platform 2) and fell below 4000 m on the valley floor with an estimated kinetic energy of 7.1×10^{13} J just before the impact. This energy exceeds the energy of 15 kt of TNT. The energy transfer caused by the sudden impact resulted in a destructive air blast and then propagated 1 km from the impact point (Kargel et al. 2016). The coupled simulation results also confirmed this viewpoint as the destructive air blast was generated at the impact point of the debris avalanche and the slope. The Langtang village fortunately avoided the impact of avalanche, but was still damaged by the generated air blast. Avalanches with an airborne trajectory could achieve extremely high energy without the energy loss from friction, releasing a large proportion of the energy instantly and thus leading to a powerful air blast.


Fig. 8 Maximum velocity contour of the air blast, showing the vertical impact region. **a**, **b**, **c** The maximum velocity contour in the horizontal section at 50 m, 150 m, and 500 m height above the valley floor, respectively

We further designed a generalized model to investigate the contribution of valley morphology to the initiation of avalanche-induced air blasts. The model geometry is controlled by three groups of planes (named planes 1, 2, and 3 from left to right) and slope angles (θ_1–θ_3), as shown in Fig. 9. θ_1 controls the acceleration of the sliding mass and provides its initial momentum. θ_2 represents a transition platform to lead the particles to the airborne point, and θ_3 controls the airborne trajectory. Our model covers the valley morphology of most avalanches (without bending in movement path) by modifying the slope angles. Figure 9a–d shows the contribution of θ_1–θ_3 to the generation of the air blast. The combination of θ_1 and θ_2 governs the mobility of avalanche before reaching the airborne trajectory. As shown in Fig. 9a and b, a steep plane 1 with a flat platform (plan 2) leads to a high initial velocity. Yet the impact with the platform releases a large proportion of energy, and parts particles even stop on the platform. Such cases can lead to no airborne motion at all or cause a relatively weak air blast at the end of the airborne trajectory. However, a smooth transition between planes 1 and 2 can improve the avalanche's mobility (Fig. 9c). When θ_1 is close to θ_2 and plane 2 (platform) has a moderate slope angle, the avalanche will not dissipate much energy at the transition point and can reach the airborne trajectory with a high velocity. The effect of θ_3 is presented in Fig. 9c and d. The rapidly moving avalanche has a greater airborne distance when combined with a steeper angle θ_3, since the materials directly land at the horizontal surface. We can clearly observe the significant contribution of airborne trajectory to the air blast generation by comparing the results of Fig. 9c and d. Though two groups of avalanches show

the same volume, elevation difference, and initial velocity (before entering plane 3), a much more powerful air blast is identified in the airborne geomorphology. The model with an airborne trajectory ($\theta_3 = 90°$; Fig. 9c) shows a maximum air blast velocity of ~10 m/s and a propagation distance of over 25 m, while the air blast in another scenario ($\theta_3 = 45°$; Fig. 9d) only has a maximum velocity of 6 m/s and a travel distance of 10 m. The avalanche experienced a free-fall motion without much friction-caused energy dissipation, and thus reached a high velocity and caused a powerful air blast at the impact. Furthermore, fall height is another important geomorphological aspect that greatly influences air blast generation. As shown in Fig. 9c and e, the results indicated that an increment in the fall height of 50% could produce ~30% powerful results for the air blast. A large fall height implies high potential energy for avalanche in the initial stage, and its combination with specific slope angles (θ_1–θ_3) will generate a destructive air blast.

Notably, the debris avalanche becoming airborne is not the only form that could release tremendous energy instantly and generate an air blast. Our previous work on the Wenjia valley debris avalanche shows another phenomenon (Zhuang et al. 2019). The Wenjia Valley debris avalanche has a complex runout path as the movement direction changes several times with the topography. Both field investigation and numerical results show that the most significant air blast was identified at each turning point of the valley. The debris avalanche with high velocity violently collided with the valley during the movement process and then caused the powerful air blast. Interestingly, the Langtang debris avalanche-induced air blast observed at platform 2 (Fig. 4b) shows a similar behavior as the air blast was
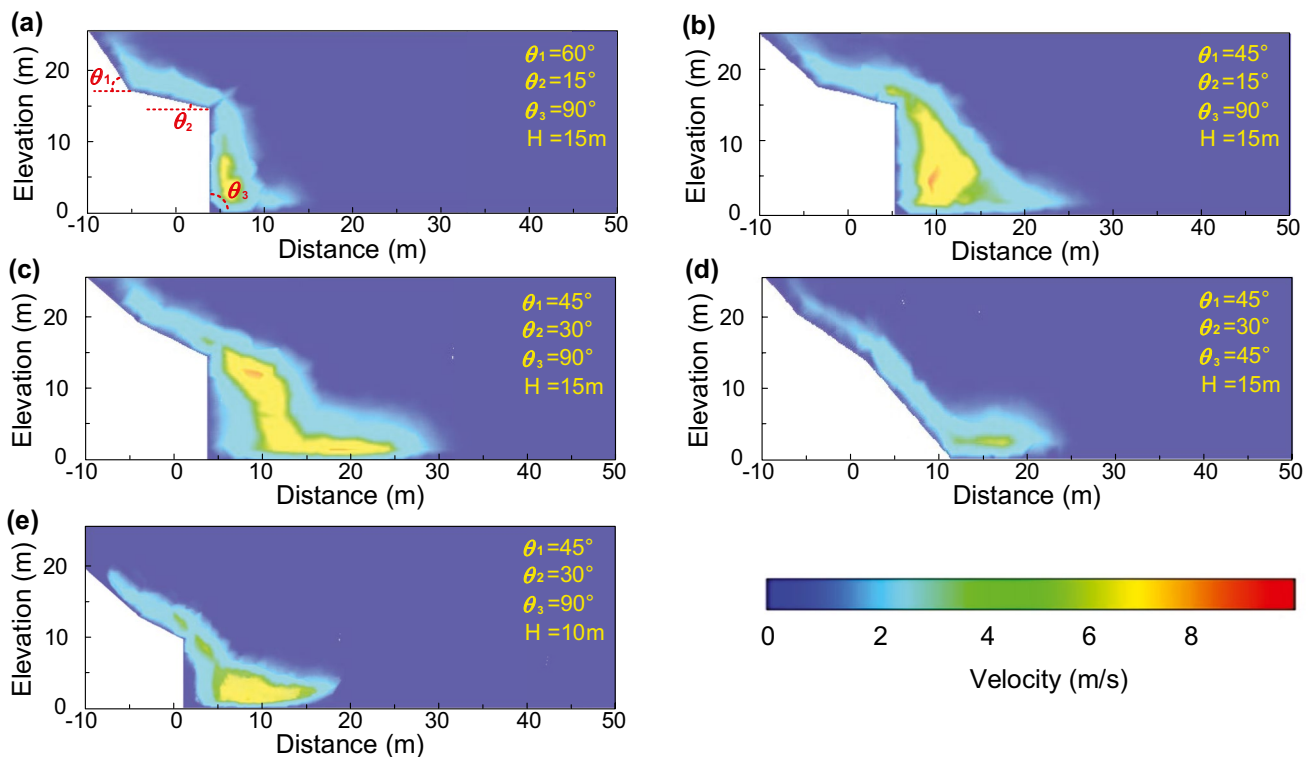
Fig. 9 Contribution of airborne geomorphology on the initiation of the avalanche-induced air blast. **a–d** The air blast generated by varying θ_1, θ_2, and θ_3, respectively. **e** The contribution of plane 3 fall height
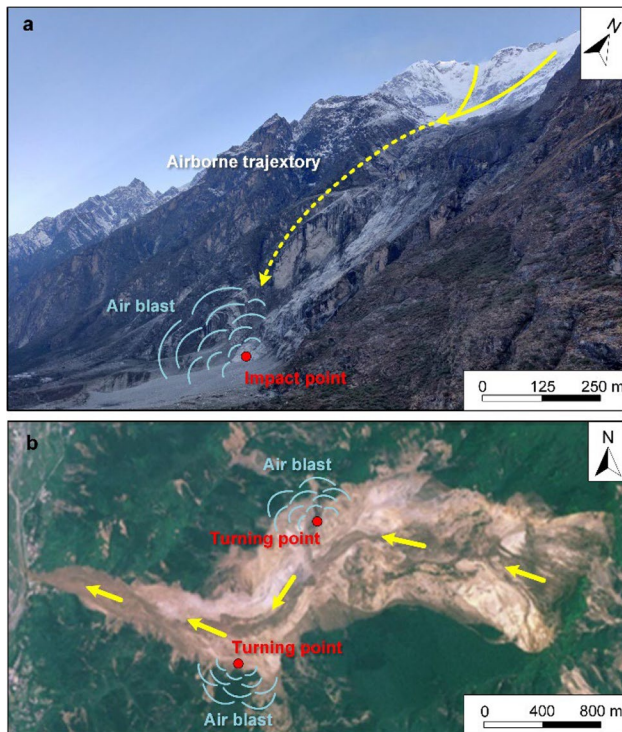
Fig. 10 Two generation modes of the avalanche-induced air blast. **a** Avalanche with an airborne trajectory (e.g. Langtang avalanche, the airborne trajectory is drawn according to Kargel et al. (2016)). **b** Avalanche runout path with turning points (e.g. Wenjia valley landslide). Yellow line indicates the movement path of the sliding mass

generated due to the impact of the avalanche on the rock mass (or two branches of avalanches). This cascading effect was located in the avalanche travel path with an extremely high altitude and no buildings or vegetation in the damage region, thus causing no casualties and was not identified in-situ. Summarily, to our knowledge, an air blast disaster is more likely from the avalanche with an airborne trajectory or occurs in the valley with turning points, as shown in Fig. 10.

Previous investigation on the typical ice/rock avalanche-induced air blasts worldwide also confirmed our viewpoints. We summarized recent typical avalanche-induced air blasts in Table 2. The Elm, Yigong, and Yumthang events are all typical avalanches that have an airborne trajectory and generate a powerful air blast. Large avalanches with airborne trajectories will not experience the frictional resistance caused by the interaction with the ground, and thus, a large proposal of energy is convertible to kinetic energy. Subsequently, the moving materials with an extremely high velocity violently collide with the ground surface and generate a destructive air blast. Such an initiation mechanism is quite similar to the bomb-induced air blast. Furthermore, similar to the Wenjia valley avalanche, the Zhaotong, Niumian valley, and Chamoli events are long runout cases with turning points in the travel path. Previous investigation results indicated that areas most seriously damaged by the air blast are near the turning points (Xing et al. 2015, 2016; Shugar et al. 2021). After impact with the valley wall, large avalanches with high velocity change the moving direction while numerous energy and momentum greatly attenuate during the stage. Meanwhile, the suddenly released energy will transmit to the surrounding air and thus generate a destructive air blast capable of causing destruction far beyond the avalanche region. These two initiation modes of the avalanche-induced air blast both involve a sudden release of energy. Thus, except for the large volume and elevation difference (causing high velocity) that is commonly observed in a long runout avalanche, the valley morphology also significantly contributes to generating a destructive air blast.

Propagation process and the extent of damage

Regarding the propagation process and the extent of damage, the avalanche-induced air blast could cause fatalities and destruction far beyond the runout of debris itself. The modeled Langtang air blast results show an initial velocity of more than 80 m/s and a propagation velocity over 40 m/s within 1 km along the valley and on the opposite slope. The generated air blast resulted in destruction comparable with an EF2–EF5 tornado, indicating its damaging impact. Furthermore, the velocity of the generated air blast is

Table 2 Typical avalanche-induced air blasts in recent years

Generation mode	Event	Impact
Avalanche with an airborne trajectory	Elm avalanche	People and wooden houses were blown up (Heim 1932)
	Yigong avalanche	Some trees with a diameter of approximately 1 m were hacked in half (Yin and Xing 2012)
	Yumthang avalanche	Flattened and snapped a forest (Penna et al. 2021)
	Langtang avalanche	Trees were fallen down on the opposite side north-facing slope and buildings in the village were damaged (Kargel et al. 2016)
Avalanche runout path with turning points	Zhaotong avalanche	Flattened crops and light damage to a roof (Xing et al. 2016)
	Wenjia Valley avalanche	Blow down the trees on both sides and front margin of the debris avalanche (Zhuang et al. 2019)
	Niumian Valley avalanche	Uprooted, snapped and scraped trees (Xing et al. 2015)
	Chamoli avalanche	Uprooted and snapped trees (Shugar et al. 2021)

quite high during the whole propagation process, even hundreds of meters away from the birthplace, showing a great difference from the rockfall-induced air blast. Morrissey et al. (1999) analyzed the propagation process of the air blast caused by the Happy Isles event, and identified a great attenuation of the wind speed (110 m/s near the impact point to 20 m/s at a distance of 400 m). This phenomenon confirmed the significant contribution of the impact duration. Compared with the rockfall-induced air blast, the long impact duration of the avalanche caused the high velocity of the generated air blast during the propagation process and a possible larger damage region. The dissipation process of air blast will start when the main impact of the avalanche finishes (Fig. 7). Notably, the air blast induced by the Langtang debris avalanche is still powerful even 1 km away from the impact point. Energy transfer resulting from the high-speed impact coupled with the narrow tomography of Langtang valley eventually caused this powerful far-field air blast. Regarding the high speed and far-affected area of the air blast, no time for people to evacuate from the damage region after the event occurs. Moreover, the vertical impact region of the air blast is also worthy of attention. The numerical results show that the Langtang avalanche-induced air blast is still powerful even at several hundred meters height about the ground, which could destroy the possible bridges (with a large vertical clearance). This phenomenon needs to be highly valued, especially for infrastructure planning in high-altitude regions (e.g. high-speed railways and bridges in Qinghai Tibet Plateau, southwest China). Thus, the avalanche-induced air blast should be a part of the geo-disaster risk assessment in these regions because of its rapid propagation and powerful far-field destruction (both horizontal and vertical).

At present, the air blast characteristics are still hard observable in situ through video or monitoring equipment because of its powerful destructed force and far-field effect. More numerical and post-disaster field work should be performed further to investigate the disaster-causing process of the avalanche-induced air blast. It will provide valuable information for preventing and mitigating such disasters in high-altitude regions. Nevertheless, the application of the numerical method was not fully paid in previous studies (Morrissey et al. 1999; Zhuang et al. 2019). The 3D DEM-CFD coupled method employed in work provides an excellent technique for the following research. Employing a three-dimensional coupled numerical model that incorporates the real geological features could provide relatively realistic results and represent the essential processes of the debris avalanche and associated air blast. That will provide insights into understanding the disaster-causing mechanism of the avalanche-induced air blast and the proposition of appropriate measures. Moreover, our future work will focus on more avalanche-induced air blast cases, analyze the relationship between possible control factors with the air blast extent, provide broader implications for such type of cascading event, and eventually establish an experimental relationship between the extent of air blasts with control factors for the risk assessment.

Conclusions

Air blasts can intensify the potential destruction by avalanches far beyond the moving mass. The destructive air blast caused by the Langtang avalanche provided a natural material for a detailed study of the avalanche induced-air blast in high-altitude regions. We analyzed the initiation and propagation process of this famous event using a DEM-CFD coupled method, and compared it with recorded events from around the world. Our work highlighted the great contribution of valley morphology. Not all avalanches trigger a significant air blast. Destructive air blasts can occur when large avalanches suddenly release tremendous energy. Besides a large volume and high velocity, special topography is also essential. Large avalanches with an airborne trajectory or a travel path with turning points are two typical scenarios for generating destructive air blasts. Furthermore, numerical results indicate the power and extension of the avalanche-induced air blast. The Langtang air blast propagated 1 km from the impact point, caused destruction comparable with an EF2–EF5 tornado, and left no time for people to escape. The long impact duration of the avalanche results in a different propagation characteristic of air blasts from that of a large rockfall, and leads to a probable longer extension. The large damage region and destruction of avalanche-induced air blasts reveal the risks faced by the rapid infrastructure expansion in high-altitude regions. This cascading effect needs to be a part of landslide risk assessment and taken into account for the long-term sustainability of planned infrastructure.

Declarations

Competing interests   The authors declare no competing interests.

References

Adams J (1881) Earthquake-dammed lakes in New Zealand. Geology 9:215–219

ANSYS Inc (2018) Ansys fluent user's guide 18.0. Pennsylvania, USA

Bartelt P, Bebi P, Feistl T, Buser O, Caviezel A (2018) Dynamic magnification factors for tree blow-down by powder snow avalanche air blasts. Nat Hazard 18(3):759–764

Bartelt P, Buser O, Vera Valero C, Bühler Y (2016) Configurational energy and the formation of mixed flowing powder snow and ice avalanches. Ann Glaciol 57(71):179–188

Bilal M, Xing AG, Zhuang Y, Zhang YB, Jin KP, Zhu YQ, Leng YY (2021) Coupled 3D numerical model for a landslide-induced impulse water wave: a case study of the Fuquan landslide. Eng Geol 290:106209

Buser O, Bartelt P (2015) An energy-based method to calculate streamwise density variations in snow avalanches. J Glaciol 61:563–575

Caviezel A, Margreth S, Ivanova KA, Sovilla B, Bartelt P (2021) Powder snow impact of tall vibrating structures. Compdyn 2021 8th ECCOMAS Thematic Conference on Computational Methods in Structural Dynamics and Earthquake Engineering, 19112

Christen M, Kowalski J, Bartelt P (2010) RAMMS: numerical simulation of dense snow avalanches in three-dimensional terrain. Cold Reg Sci Technol 63:1–14

Collins BD, Jibson RW (2015) Assessment of existing and potential landslide hazards resulting from the April 25, 2015 Gorkha, Nepal Earthquake Sequence. U.S. Geol Surv Open-File Rep 2015–1142

De Blasio, Dattola FV, Crosta GB (2018) Extremely energetic rockfalls. J Geophys Res Earth Surf 123:2392–2421

DEM Solutions Ltd (2019) EDEM 2018 user guide, Edinburgh, UK

Dreier L, Bühler Y, Ginzler C, Bartelt P (2016) Comparison of simulated powder snow avalanches with photogrammetric measurements. Ann Glaciol 57(71):371–381

ESRI Inc (2019) ArcGIS 10.7, Redlands, CA

Fujita K, Inoue H, Izumi T, Yamaguchi S, Sadakane A, Sunako S, Nishimura K, Immerzeel WW, Shea JM, Kayastha RB, Sawagaki T, Breashears DF, Yagi H, Sakai A (2017) Anomalous winter-snow-amplified earthquake-induced disaster of the 2015 Langtang avalanche in Nepal. Nat Hazards Earth Syst Sci 17:749–764

Gao NS, Zhang ZC (2021) Optimization design and experimental verification of compositeabsorber with broadband and high efficiency sound absorption. Appl Acoust 183:108288

Gnyawali KR, Xing AG, Zhuang Y (2020) Dynamic analysis of the multi-staged ice-rock debris avalanche in the Langtang valley triggered by the 2015 Gorkha earthquake. Nepal Eng Geol 265:105440

He K, Chen C, Li B (2018) Case study of a rockfall in Chongqing, China: movement characteristics of the initial failure process of a tower-shaped rock mass. Bull Eng Geol Env 78:3295–3303

Heim A (1932) Bergsturz und Menschenleben. Fretz & Wasmuth, Ziirich

Hertz H (1882) Ueber die Berührung fester elastischer Körper. Journal Für Die Reine Und Angewandte Mathematik 92:156–171

Houghton EL, Carpenter PW (2003) Aerodynamics for engineering students. Elsevier, Britain, pp 62–67

Kargel JS et al (2016) Geomorphic and geologic controls of geohazards induced by Nepal's 2015 Gorkha earthquake. Science 351:aac8353

Lacroix P (2016) Landslides triggered by the Gorkha earthquake in the Langtang valley, volumes and initiation processes. Earth Planet Space 68:46

Mindlin R (1949) Compliance of elastic bodies in contact. J Appl Mech 16:259–268

Morrissey MM, Wieczorek GF, Savage WZ (1999) Airblasts generated from rock-fall impacts: analysis of the 1996 Happy Isles event in Yosemite National Park. Journal of Geophysical Research: Solid Earth 104:23189–23198

Mulligan RP, Franci A, Celigueta MA, Take WA (2020) Simulations of landslide wave generation and propagation using the particle finite element method. J Geophys Res Oceans 125:e2019JC015873

Nagai H, Watanabe M, Tomii N, Tadono T, Suzuki S (2017) Multiple remote-sensing assessment of the catastrophic collapse in Langtang Valley induced by the 2015 Gorkha earthquake. Nat Hazard 17:1907–1921

Ni J, Wu T, Zhu X, Wu X, Qiao Y (2021) Risk assessment of potential thaw settlement hazard in the permafrost regions of Qinghai-Tibet Plateau. Sci Total Environ 776:145855

Penna IM, Hermanns RL, Nicolet P, Morken OA, Jaboyedoff M (2021) Air-blasts caused by large slope collapses. Geol Soc Am Bull 133:939–948

Shugar DH et al (2021) A massive rock and ice avalanche caused the 2021 disaster at Chamoli, Indian Himalaya. Science 373:eabh4455

Skiles SM, Painter T (2017) Daily evolution in dust and black carbon content, snow grain size, and snow albedo during snowmelt, Rocky Mountains. Colorado J Glaciol 63(237):118–132

Wang FW, Cheng QG, Highland L, Miyajima M, Wang HB, Yan CG (2009) Preliminary investigation of some large landslides triggered by the 2008 Wenchuan earthquake, Sichuan province, China. Landslides 6:47–54

Wieczorek GF, Snyder JB, Waitt RB, Morrissey MM, Uhrhammer RA, Harp EL, Norris RD, Bursik M, Finewood LG (2000) Unusual July 10, 1996, rock fall at Happy Isles, Yosemite National Park, California. Geol Soc Am Bull 112:75–85

Xing AG, Wang GH, Yin YP, Tang C, Xu ZM, Li WL (2016) Investigation and dynamic analysis of a catastrophic rock avalanche on September 23, 1991, Zhaotong, China. Landslides 13:1035–1047

Xing AG, Xu Q, Can JJ (2015) On characteristics and dynamic analysis of the Niumian valley rock avalanche triggered by the 2008 Wenchuan earthquake, Sichuan, China. Environ Earth Sci 73:3387–3401

Yakhot V, Orszag SA (1986) Renormalization group analysis of turbulence I. Basic theory. J Sci Comput 1:3–51

Yin YP (2014) Vertical acceleration effect on landsides triggered by the Wenchuan earthquake, China. Environ Earth Sci 71:4703–4714

Yin YP, Xing AG (2012) Aerodynamic modeling of the yigong gigantic rock slide-debris avalanche, Tibet, China. Bull Eng Geol Env 71:149–160

Zhang KQ, Wang LQ, Dai ZW, Huang BL, Zhang ZH (2022) Evolution trend of the Huangyanwo rock mass under the action of reservoir water fluctuation. Nat Hazards. https://doi.org/10.1007/s11069-022-05359-y

Zhuang Y, Xing AG, Leng YY, Bilal M, Zhang YB, Jin KP, He JY (2021) Investigation of characteristics of long runout landslides based on the multi-source data collaboration: a case study of the Shuicheng Basalt landslide in Guizhou, China. Rock Mech Rock Eng 54:3783–3798

Zhuang Y, Xu Q, Xing AG (2019) Numerical investigation of the air blast generated by the Wenjia valley rock avalanche in Mianzhu, Sichuan, China. Landslides 16:2499–2508

Zimmer VL, Collins BD, Stock GM, Sitar N (2012) Rock fall dynamics and deposition: an integrated analysis of the 2009 Ahwiyah Point rock fall, Yosemite National Park, USA. Earth Surf Proc Land 37:680–691

Yu Zhuang · Aiguo Xing · Muhammad Bilal
State Key Laboratory of Ocean Engineering, Shanghai Jiao Tong University, Shanghai 200240, People's Republic of China

Yu Zhuang · Qiang Xu (✉)
State Key Laboratory of Geohazard Prevention and Geoenvironment Protection, Chengdu University of Technology, Chengdu 610059, China
Email: xq@cdut.edu.cn

Kaushal Raj Gnyawali
School of Engineering, University of British Columbia, Kelowna, BC, Canada